Available online at www.sciencedirect.com
ScienceDirect
Journal of Computational Physics 227 (2008) 7621–7642
JOURNAL OF COMPUTATIONAL PHYSICS
www.elsevier.com/locate/jcp

Upscaling methods for a class of convection–diffusion equations with highly oscillating coefficients ☆

Weibing Deng *, Ji Gu, Jianmin Huang

Department of Mathematics, Nanjing University, Nanjing 210093, People's Republic of China

Received 7 January 2008; received in revised form 21 April 2008; accepted 24 April 2008
Available online 15 May 2008

Abstract

This paper investigates the upscaling method to the following parabolic equation:

$$\partial_t c + \nabla \cdot (\mathbf{u}c) - \nabla \cdot (\mathbf{D}\nabla c) = f(x,t),$$

which stems from the application of solute transport in porous media. Because of the highly oscillating permeability of the porous media, the Darcy velocity **u** hence the dispersion tensor **D** has many scales with high contrasts. Thus, how to calculate the macro-scale equivalent coefficients of the above equation becomes the target of this paper. A new upscaling method is proposed and studied via comparing with another upscaling method which was proposed in [Z. Chen, W. Deng, H. Ye, Discrete Contin. Dyn. Syst. 13 (2005), 941–960]. The two different equivalent coefficients computing formulations are based on the solutions of two different cell (local) problems, which one utilizes the elliptic operator with terms of all orders while the other only uses the second order term. Error estimates between the equivalent coefficients and the homogenized coefficients are given under the assumption that the oscillating coefficients are periodic (which is not required by the method). Numerical experiments are carried out for the periodic coefficients to demonstrate the accuracy of the proposed method. Moreover, the upscaling method is applied to solve the solute transport in a porous medium with a random log-normal relative permeability. The results show the efficiency and accuracy of the proposed method.

MSC: 74Q99; 76R99; 76S05

Keywords: Upscaling method; Solute transport equation; Cell problem

☆ This work is partially supported by the National Natural Science Foundation of China under the grant 10501022 and also supported by the Natural Science Foundation of Jiang Su under the grant BK2006511.
* Corresponding author.
E-mail address: wbdeng@nju.edu.cn (W. Deng).

0021-9991/$ - see front matter © 2008 Elsevier Inc. All rights reserved.
doi:10.1016/j.jcp.2008.04.037

1. Introduction

1.1. Research background

In this paper, we consider a two-dimensional horizontal aquifer where gravity effects are negligible. Assuming that the aquifer porous medium has a constant porosity, the single-phase flow of an incompressible fluid with a dissolved solute in a horizontal porous aquifer $\Omega \in \mathbb{R}^2$ over a time period $J = [T_0, T_1]$, is given by (see [16])

$$-\nabla \cdot (\mathbf{K}^\varepsilon \nabla p^\varepsilon) = \nabla \cdot \mathbf{u}^\varepsilon = q, \quad x \in \Omega \tag{1.1}$$

and

$$\frac{\partial c}{\partial t} - \nabla \cdot (\mathbf{D}^\varepsilon \nabla c - \mathbf{u}^\varepsilon c) = f, \quad x \in \Omega, \ \ t \in J, \tag{1.2}$$

where q is the source or sink of fluid, $\mathbf{K}^\varepsilon(x)$ is the permeability tensor which is symmetric and positive definite (assuming unit viscosity), p^ε is the fluid pressure, $\mathbf{u}^\varepsilon(x) = (u_i)$ is the pore-scale velocity vector, $c(x,t)$ is the concentration of the contaminant solute, and $\mathbf{D}^\varepsilon = (d_{ij})$ is the pore-scale dispersion tensor. Note that ε is a small parameter indicating the length of the small scales. The form of the diffusion–dispersion tensor $\mathbf{D}^\varepsilon$ is given by (see [16,32])

$$d_{ij} = \alpha_T |\mathbf{u}^\varepsilon| \delta_{ij} + (\alpha_L - \alpha_T) \frac{u_i u_j}{|\mathbf{u}^\varepsilon|}, \quad |\mathbf{u}^\varepsilon| = \sqrt{u_i^2}, \tag{1.3}$$

where α_L and α_T are the longitudinal and transverse dispersion coefficients respectively. In general $\alpha_L \approx 10\alpha_T$, but this may vary greatly with different soils, fractured media, etc.

Owing to complex heterogeneity of natural media and scarcity of the available field data, the permeability filed, $\mathbf{K}^\varepsilon(x)$, is a randomly varying coefficient with potentially large contrasts. The direct numerical simulation of these problems is difficult because of limited computer power and memory. On the other hand, in practice, it is often sufficient to predict the macroscopic properties of the solutions to a certain accuracy. Thus, various methods of upscaling or homogenization have been developed which approximate the original governing equations by another, often of the same form, with known coefficients that can be solved with fewer computing resources (see the review papers [17,30,34] and references therein). The main idea of the upscaling methods is to lump the small-scale details of the medium into a few representative macroscopic parameters or effective parameters on a coarse scale which preserve the large-scale behavior of the medium. This idea is essentially the same as the representative volume element method (RVE). Many kinds of multiscale methods have been done based on similar ideas. See, for instance, the generalized finite element method [3,4], the multiscale finite element method [15,22], the wavelet homogenization techniques [11], the multigrid numerical homogenization techniques [27], the subgrid upscaling method [2], and the heterogeneous multiscale method [13,14]. We refer the reader to [26] for an overview of the above methods.

However, to our knowledge, in the literature most of the upscaling methods are proposed to problem (1.1); while, there are not so many works on how to derive an upscaling equation for the solute transport Eq. (1.2) (see the books [21,28] for some works concerning the upscaling of convection–diffusion equation). It is easy to see that in our considered system, $\mathbf{u}^\varepsilon(x)$ hence $\mathbf{D}^\varepsilon(x)$ are strongly varying coefficients because of the variability of $\mathbf{K}^\varepsilon(x)$. Thus, how to find an equivalent equation to (1.2) in the macro-scale is still important for the simulation of solute transport model. In this paper, we therefore focus our attention on (1.2), and try to give a positive answer to how to calculate the upscaling (equivalent) coefficients for it.

In [8], a new upscaling method was introduced to solve the solute transport Eq. (1.2). The method incorporates the upscaling procedure into the implementing of the finite element method, which can be considered as the implementation of the generalized finite element method (see [4, pp. 513–514]). We remark that the idea to modify the original finite element equation (see [4, p. 513. Eq. (3.2)]) has been used in many other works such as the finite element method based on the residual-free bubble method (or the variational multiscale method, discontinuous enrichment method) [7,18,19,24,31]. The interesting part of the method proposed in [8] is that the effective coefficients, both the diffusivity and velocity, are computed by using the solutions of

the same local problems which are second order elliptic equations that only use the fine scale information of the diffusion coefficient. In this paper, we give a different effective coefficients computing method based on the solutions of the cell problems which use the fine scale information of the diffusion and convection coefficients simultaneously. We found that this new method can be applicable to more general case and has a better performance in accuracy. It has to be emphasized that the new method is also developed on the same idea as above. However, it focuses on how to use the fine scale information to compute the effective coefficients, especially there is a convection term. We give the details of the implementing procedure which are new in our opinion.

1.2. Understanding of the two-stage upscaling procedure

To (1.1), the main result of upscaling is often the block permeability, a constant tensor computed in each grid block. In [17], the upscaling techniques are described as two-stage procedures. In the first stage – the fine grid experiment – one or more fine grid problems are solved. In the second stage – the coarse scale calibration – the fine grid solutions are used to determine the coarse scale properties. Via the two-stage procedure, an effective representation of the permeability on a coarse mesh is found so that the large scale flow can be correctly computed on this mesh. The computational cost is thus greatly reduced. Following the two-stage procedure, we recall the so-called local Laplacian formulations here (see also [29,35]) and try to motivate the upscaling method for the solute transport equation. The method is done as follows. In the first stage, for a given grid block V, we solve the following equation:

$$\nabla \cdot \mathbf{u}^\varepsilon = 0, \quad \mathbf{u}^\varepsilon = -\mathbf{K}^\varepsilon \nabla p^\varepsilon, \ \ x \in V,$$

with appropriate boundary conditions (see [35] for more details). Further, in the second stage, we define the block (upscaling) permeability, $\widetilde{\mathbf{K}}$, such that

$$\widetilde{\mathbf{K}} \langle \nabla p^\varepsilon \rangle_V = -\langle \mathbf{u}^\varepsilon \rangle_V, \tag{1.4}$$

where p^ε and $\mathbf{u}^\varepsilon$ are the solutions we computed in the first stage. Here $\langle \cdot \rangle_V$ represents the mean value of a function in the domain V, i.e.,

$$\langle \cdot \rangle_V = \frac{1}{|V|} \int_V (\cdot) \mathrm{d}x.$$

A rigorous analysis of the upscaling error between the effective permeability of the medium, $\mathbf{K}^*$ and the block permeability, $\widetilde{\mathbf{K}}$ is provided in the paper [35]. The local Laplacian methods are founded on the properties of $\mathbf{K}^*$ such that [25,35] (1) it is unique; (2) it is independent of the source term and of the boundary condition on $\partial\Omega$; and (3) it can be determined locally, i.e., to determine $\mathbf{K}^*$ at a point $x \in \Omega$, one needs only to consider (1.1) in the neighborhoods of x. An intrinsic connection between $\mathbf{K}^*$ and $\widetilde{\mathbf{K}}$ is also given in [35, p.188].

Motivated by the above observation, we try to give a similar definition of the equivalent coefficients to Eq. (1.2). Following the two-stage procedure, it is defined as follows. In the first stage, for a given grid block V, we solve the following equation:

$$\nabla \cdot \mathbf{v}^\varepsilon = 0, \quad \mathbf{v}^\varepsilon = \mathbf{u}^\varepsilon c^\varepsilon - \mathbf{D}^\varepsilon \nabla c^\varepsilon, \ \ x \in V,$$

with appropriate boundary conditions. Further, in the second stage, we define the upscaling coefficients, $\widetilde{\mathbf{D}}$ and $\tilde{\mathbf{u}}$, such that

$$-\tilde{\mathbf{u}} \langle c^\varepsilon \rangle_V + \widetilde{\mathbf{D}} \langle \nabla c^\varepsilon \rangle_V = -\langle \mathbf{v}^\varepsilon \rangle_V, \tag{1.5}$$

where c^ε and $\mathbf{v}^\varepsilon(x)$ are the solutions we computed in the first stage.

We restate the key point here for the convenience of the reader (see [35, p. 188]). According to the homogenization theory, the effective coefficients, $\mathbf{u}^*$ and $\mathbf{D}^*$, are defined through the following criteria [6,25]: for any measurable $V \in \Omega$:

$$\lim_{\varepsilon \to 0} \langle \nabla c^\varepsilon \rangle_V = \langle \nabla c \rangle_V, \quad \lim_{\varepsilon \to 0} \langle \mathbf{v}^\varepsilon \rangle_V = \langle \mathbf{v} \rangle_V, \quad \lim_{\varepsilon \to 0} c^\varepsilon = c, \tag{1.6}$$

where c and $\mathbf{v}$ are the solutions of the effective (or homogenized) equation

$$\nabla \cdot (\mathbf{u}^* c - \mathbf{D}^* \nabla c) = \nabla \cdot \mathbf{v} = 0, \quad x \in V. \tag{1.7}$$

It is easy to see that $\tilde{\mathbf{u}}$ and $\widetilde{\mathbf{D}}$ are approximations of $\mathbf{u}^*$ and $\mathbf{D}^*$ respectively. More specifically, consider a point $x \in \Omega$ and grid block $V \in \Omega$ containing x. From (1.5), (1.6) and (1.7), we have

$$\langle \mathbf{v}^\varepsilon \rangle_V \approx \lim_{\varepsilon \to 0} \langle \mathbf{v}^\varepsilon \rangle_V = \langle \mathbf{u}^* c \rangle_V - \langle \mathbf{D}^* \nabla c \rangle_V \approx \mathbf{u}^*(x) c - \mathbf{D}^*(x) \nabla c,$$

$$\langle c^\varepsilon \rangle_V \approx \lim_{\varepsilon \to 0} \langle c^\varepsilon \rangle_V = \langle c \rangle_V, \quad \langle \nabla c^\varepsilon \rangle_V \approx \lim_{\varepsilon \to 0} \langle \nabla c^\varepsilon \rangle_V = \langle \nabla c \rangle_V.$$

Hence, $\tilde{\mathbf{u}} \approx \mathbf{u}^*(x)$ and $\widetilde{\mathbf{D}} \approx \mathbf{D}^*(x)$.

The outline of the paper is as follows. In Section 2 we introduce the new upscaling method for the model problem. In Section 3 we give the error estimate for the proposed method. In Section 4 we give some numerical examples in periodic case to verify the error estimates, and in Section 5 we apply our method to the solute transport model with a practical random log-normal permeability to demonstrate the efficiency of the upscaling method. Conclusions are drawn in the last section.

2. Upscaling formulations for model problem

In this section, we consider the following model problem:

$$\begin{cases} -\nabla \cdot (\mathbf{b}^\varepsilon(x) u^\varepsilon(x)) - \nabla \cdot (\mathbf{a}^\varepsilon(x) \nabla u^\varepsilon(x)) = f(x), & x \in \Omega, \\ u^\varepsilon(x) = 0, & x \in \partial\Omega, \end{cases} \tag{2.1}$$

where $\Omega \subset \mathbb{R}^d$, $d = 2, 3$ is a bounded polyhedral domain with a Lipschitz boundary $\partial\Omega$, and $\varepsilon \ll 1$ is a parameter that represents the ratio of the smallest and largest scales in the problem. Problems of the type (2.1) are related to groundwater and solute transport in porous media (see [10]). For problem (2.1), we assume that $f(x) \in L^2(\Omega)$, $\mathbf{a}^\varepsilon(x) = (a_{ij}^\varepsilon(x))$ is a symmetric, positive definite, bounded tensor satisfying

$$\lambda |\xi|^2 \leqslant a_{ij}^\varepsilon(x) \xi_i \xi_j \leqslant \Lambda |\xi|^2 \quad \forall \xi \in \mathbb{R}^d, \ x \in \overline{\Omega} \tag{2.2}$$

for some positive constants λ and Λ, and $\mathbf{b}^\varepsilon(x) = (b_i^\varepsilon(x))$ is a bounded vector.

Variational problem of (2.1) is to seek $u^\varepsilon(x) \in H_0^1(\Omega)$ such that

$$(\mathbf{b}^\varepsilon(x) u^\varepsilon + \mathbf{a}^\varepsilon(x) \nabla u^\varepsilon, \nabla v) = (f, v) \quad \forall v \in H_0^1(\Omega). \tag{2.3}$$

Instead of solving (2.3) on a fine mesh with a mesh size resolving the small scale variability ε, the goal of the upscaling method is to find the solution of the corresponding macro-scale equation which may have the following form:

$$(\tilde{\mathbf{b}}(x) u + \tilde{\mathbf{a}}(x) \nabla u, \nabla v) = (f, v) \quad \forall v \in H_0^1(\Omega).$$

We emphasize that in general case the coefficients $\tilde{\mathbf{a}}, \tilde{\mathbf{b}}$ cannot be calculated analytically since $\mathbf{a}^\varepsilon, \mathbf{b}^\varepsilon$ do not have the special structure such as periodicity to be used. Therefore we aim at how to calculate the upscaled coefficients $\tilde{\mathbf{a}}$ and $\tilde{\mathbf{b}}$; hence derive an "effective equation" to Eq. (1.2) and solve it on a coarse-scale mesh. To the end, let $\mathcal{M}_h$ be a regular triangulation of Ω with mesh size h much larger than the ε. Then, in each $K \in \mathcal{M}_h$, the upscaled coefficients $\tilde{\mathbf{a}} = (\tilde{a}_{ij})$ is a constant tensor, and $\tilde{\mathbf{b}} = (\tilde{b}_i)$ is a constant vector, which are defined by the following method.

UM1: Let $p_i^\varepsilon, i = 1, 2, \ldots, d, d+1$, be the solution of the problem

$$\begin{aligned} &-\nabla \cdot (\mathbf{b}^\varepsilon(x) p_i^\varepsilon + \mathbf{a}^\varepsilon(x) \nabla p_i^\varepsilon) = 0 \quad \text{in } K, \\ &p_i^\varepsilon = x_i \qquad\qquad\qquad\qquad\quad \text{on } \partial K, \end{aligned} \tag{2.4}$$

where $x_{d+1} = 1$. Then, $\tilde{\mathbf{a}}, \tilde{\mathbf{b}}$ are determined by the following system:

$$\begin{aligned} \tilde{\mathbf{a}} \langle \nabla p_i^\varepsilon \rangle_K + \tilde{\mathbf{b}} \langle p_i^\varepsilon \rangle_K &= \langle \mathbf{a}^\varepsilon(x) \nabla p_i^\varepsilon + \mathbf{b}^\varepsilon(x) p_i^\varepsilon \rangle_K, \\ &i = 1, 2, \ldots, d, d+1. \end{aligned} \tag{2.5}$$

Here and in the following we call it as the upscaling method 1 and abbreviate it as UM1. We note here that the above method is deduced by the idea we discussed in Section 1.2; see the formula (1.5). For comparison, we

also recall the upscaling method proposed in [8] here and call it as the upscaling method 2 (abbreviate as UM2) which is done as follows.

UM2: In each $K \in \mathcal{M}_h$, let $p_i^\varepsilon, i = 1, 2, \ldots, d$, be the solution of the problem

$$\begin{aligned} -\nabla \cdot (\mathbf{a}^\varepsilon(x)\nabla p_i^\varepsilon) &= 0 \quad \text{in } K, \\ p_i^\varepsilon &= x_i \quad \text{on } \partial K. \end{aligned} \tag{2.6}$$

Then, $\tilde{\mathbf{a}}$ is determined by the following system:

$$\tilde{\mathbf{a}}\langle \nabla p_i^\varepsilon \rangle_K = \langle \mathbf{a}^\varepsilon(x)\nabla p_i^\varepsilon \rangle_K, \quad i = 1, 2, \ldots, d. \tag{2.7}$$

Further, $\tilde{\mathbf{b}}$ is computed by the following formulas:

$$\tilde{b}_i = \langle \mathbf{b}^\varepsilon(x) \cdot \nabla p_i^\varepsilon \rangle_K, \quad i = 1, 2, \ldots, d. \tag{2.8}$$

Due to the definition of p_i^ε on the element boundary, we can give further simplification to the above computing formulas. Indeed, the Green's Theorem gives

$$\langle \nabla p_i^\varepsilon \rangle_K = \frac{1}{|K|} \int_{\partial K} x_i \mathbf{n} \mathrm{d}\sigma = \mathbf{e}_i, \quad i = 1, \ldots, d,$$

where $\mathbf{e}_i$ is the unit vector in the ith direction, and

$$\langle \nabla p_{d+1}^\varepsilon \rangle_K = \frac{1}{|K|} \int_{\partial K} x_{d+1} \mathbf{n} \mathrm{d}\sigma = \mathbf{0}.$$

Thus, the formulas of UM1, in the case where $d = 2$, can be rewritten as

$$\begin{pmatrix} 1 & 0 & \langle p_1^\varepsilon \rangle_K \\ 0 & 1 & \langle p_2^\varepsilon \rangle_K \\ 0 & 0 & \langle p_3^\varepsilon \rangle_K \end{pmatrix} \begin{pmatrix} \tilde{a}_{11} & \tilde{a}_{21} \\ \tilde{a}_{12} & \tilde{a}_{22} \\ \tilde{b}_1 & \tilde{b}_2 \end{pmatrix} = \begin{pmatrix} \langle \mathbf{a}^\varepsilon(x)\nabla p_1^\varepsilon + \mathbf{b}^\varepsilon(x) p_1^\varepsilon \rangle_K' \\ \langle \mathbf{a}^\varepsilon(x)\nabla p_2^\varepsilon + \mathbf{b}^\varepsilon(x) p_2^\varepsilon \rangle_K' \\ \langle \mathbf{a}^\varepsilon(x)\nabla p_3^\varepsilon + \mathbf{b}^\varepsilon(x) p_3^\varepsilon \rangle_K' \end{pmatrix}$$

which yields

$$\begin{pmatrix} \tilde{b}_1 \\ \tilde{b}_2 \end{pmatrix} = \frac{\langle \mathbf{a}^\varepsilon(x)\nabla p_3^\varepsilon + \mathbf{b}^\varepsilon(x) p_3^\varepsilon \rangle_K}{\langle p_3^\varepsilon \rangle_K} \tag{2.9}$$

and

$$\begin{pmatrix} \tilde{a}_{11} \\ \tilde{a}_{21} \end{pmatrix} = \langle \mathbf{a}^\varepsilon(x)\nabla p_1^\varepsilon + \mathbf{b}^\varepsilon(x) p_1^\varepsilon \rangle_K - \tilde{\mathbf{b}} \langle p_1^\varepsilon \rangle_K, \tag{2.10}$$

and

$$\begin{pmatrix} \tilde{a}_{12} \\ \tilde{a}_{22} \end{pmatrix} = \langle \mathbf{a}^\varepsilon(x)\nabla p_2^\varepsilon + \mathbf{b}^\varepsilon(x) p_2^\varepsilon \rangle_K - \tilde{\mathbf{b}} \langle p_2^\varepsilon \rangle_K. \tag{2.11}$$

Similarly, the formulas of UM2, in the case where $d = 2$, can be rewritten as

$$\begin{pmatrix} \tilde{a}_{11} \\ \tilde{a}_{21} \end{pmatrix} = \langle \mathbf{a}^\varepsilon(x)\nabla p_1^\varepsilon \rangle_K, \quad \begin{pmatrix} \tilde{a}_{12} \\ \tilde{a}_{22} \end{pmatrix} = \langle \mathbf{a}^\varepsilon(x)\nabla p_2^\varepsilon \rangle_K, \tag{2.12}$$

and

$$\tilde{b}_1 = \langle \mathbf{b}^\varepsilon(x) \cdot \nabla p_1^\varepsilon \rangle_K, \quad \tilde{b}_2 = \langle \mathbf{b}^\varepsilon(x) \cdot \nabla p_2^\varepsilon \rangle_K. \tag{2.13}$$

We will use the above formulas (2.9),(2.10), (2.11), (2.12), (2.13) in our later numerical experiments.

Remark 1. In both UM1 and UM2, $\tilde{\mathbf{a}}, \tilde{\mathbf{b}}$ are well-defined. Moreover, for UM2, we can show that $\tilde{\mathbf{a}}$ is symmetric positive definite and bounded. But for UM1, the symmetry does not hold. Our later numerical experiments show that when ε is small enough, the effective diffusive tenor will be asymptotically symmetric.

Remark 2. When $\mathbf{b}^\varepsilon$ is divergence free, the formula of $\tilde{\mathbf{b}}$ in UM1 is the same as that of UM2, namely, both of them can be written as

$$\tilde{b}_i = \langle b_i^\varepsilon \rangle_K, \quad i = 1, \ldots, d. \tag{2.14}$$

Indeed, for UM1, since $\nabla \cdot \mathbf{b}^\varepsilon = 0$, it is easy to check that $p_{d+1}^\varepsilon \equiv 1$ in K, which follows (2.14) from (2.5) directly. For UM2, by use of Gauss Theorem, we have:

$$\begin{aligned} \int_K \mathbf{b}^\varepsilon(x) \cdot \nabla p_i^\varepsilon \mathrm{d}x &= \int_{\partial K} \mathbf{b}^\varepsilon \cdot \mathbf{n} x_i d\sigma \\ &= \int_K \mathbf{b}^\varepsilon(x) \cdot \mathbf{e}_i \mathrm{d}x, \quad i = 1, \ldots, d, \end{aligned}$$

which yields (2.14) immediately.

3. Error estimate for periodic coefficients

In this section, we give the error estimate to the introduced upscaling method. To do this, we assume that

$$\mathbf{a}^\varepsilon(x) = \mathbf{a}(x/\varepsilon), \quad \mathbf{b}^\varepsilon(x) = \mathbf{b}(x/\varepsilon) \tag{3.1}$$

and

$$a_{ij}(y), \quad b_i(y) \in C_p^1(\mathbb{R}^d), \tag{3.2}$$

where $C_p^1(\mathbb{R}^d)$ stands for the collection of all $C^1(\mathbb{R}^d)$ periodic functions with respect to the unit cube Y. This assumption allows us to use the homogenization theory to obtain the asymptotic structure of the solutions. We emphasize that the spatial periodicity assumption does not a priori restrict the applicability of the results only to media which do exhibit such strict repetitive spatial ordering in the properties of interest. The numerical experiments in Section 5 indicate that our method works fine for the well-accepted random log-normal permeability models in the engineering literature.

Under the assumptions (3.1) and (3.2), it is shown that u^ε converges to the solution of the homogenized equation (cf. [6,25])

$$\begin{aligned} -\nabla \cdot (\mathbf{b}^* u + \mathbf{a}^* \nabla u) &= f(x) \quad \text{in } \Omega, \\ u(x) &= 0 \quad \text{on } \partial\Omega, \end{aligned} \tag{3.3}$$

where

$$a_{ij}^* = \frac{1}{|Y|} \int_Y a_{ik}(y) \left(\delta_{kj} + \frac{\partial \chi^j}{\partial y_k}(y) \right) \mathrm{d}y. \tag{3.4}$$

Here χ^j is the periodic solution of

$$-\nabla_y \cdot (\mathbf{a}(y) \nabla_y \chi^j(y)) = \nabla_y \cdot (\mathbf{a}(y) \mathbf{e}_j), \quad j = 1, \ldots, d \tag{3.5}$$

with zero mean, i.e., $\int_Y \chi^j \mathrm{d}y = 0$. Furthermore,

$$b_i^* = \frac{1}{|Y|} \int_Y \left(b_i(y) + a_{ik} \frac{\partial \eta}{\partial y_k}(y) \right) \mathrm{d}y, \tag{3.6}$$

where η is the periodic solution of

$$-\nabla_y \cdot (\mathbf{a}(y) \nabla_y \eta(y)) = \nabla_y \cdot \mathbf{b}(y) \tag{3.7}$$

with zero mean, i.e., $\int_Y \eta \mathrm{d}y = 0$.

Based on the above homogenization theory, we can show the following error estimate result for UM1.

Theorem 3.1. *Given domain K with $diam(K) = h$ and $\tilde{\mathbf{a}}, \tilde{\mathbf{b}}$ are computed by the formulations of UM1, then we have the following error estimates*:

$$\left| a_{ij}^* - \tilde{a}_{ij} \right| \leqslant C_1 h + C_2 \varepsilon + C_3 \frac{\varepsilon}{h}, \quad i, j = 1, \ldots, d \tag{3.8}$$

and

$$|b_i^* - \tilde{b}_i| \leqslant C_1\varepsilon + C_2\frac{\varepsilon}{h}, \quad i = 1, \ldots, d, \tag{3.9}$$

where C_1, C_2, C_3 are independent of ε and h.

We arrange the proof in the Appendix for the interested reader. Further, we state the error estimate result for UM2 as follows (see [8, Lemma 4. and 5.]).

Theorem 3.2. *Given domain K with $diam(K) = h$ and $\tilde{\mathbf{a}}, \tilde{\mathbf{b}}$ are computed by the formulations of UM2, then we have the following error estimates*:

$$|a_{ij}^* - \tilde{a}_{ij}| \leqslant C\frac{\varepsilon}{h}, \quad i, j = 1, \ldots, d \tag{3.10}$$

and

$$|b_i^* - \tilde{b}_i| \leqslant C\frac{\varepsilon}{h}, \quad i = 1, \ldots, d, \tag{3.11}$$

where C is independent of ε and h.

Remark 3. We note that the error estimate bounds of UM1 have two extra terms of h and ε than UM2 does. However, our later numerical experiments show that comparing to the error term ε/h, the effect of the h term is very small, and almost cannot be found in the tests. It seems that we overestimate the errors in the theoretical proof.

4. Accuracy of UM1 and UM2

The aim of this section is to verify the error estimates (3.8), (3.9), (3.10), and (3.11). To do this, we consider the model problem (2.1) in the domain $\Omega = (0,1) \times (0,1)$, and assume that the coefficients $\mathbf{a}^\varepsilon(x_1, x_2)$ and $\mathbf{b}^\varepsilon(x_1, x_2)$ have the following periodic forms:

$$\mathbf{a}^\varepsilon(x_1, x_2) = \mathrm{Diag}(1/[2 + P_1 \sin(2\pi(2x_1 - x_2)/\varepsilon)]) \tag{4.1}$$

and

$$\mathbf{b}^\varepsilon(x_1, x_2) = \begin{pmatrix} 1/[2 + P_1 \sin(2\pi(4x_1 - x_2)/\varepsilon)] \\ 1/[2 + P_2 \sin(2\pi(x_1 + 3x_2)/\varepsilon)] \end{pmatrix}. \tag{4.2}$$

We fix $P_1 = 1.8, P_2 = 1.6$. Then the exact effective coefficients $\mathbf{a}^*$ and $\mathbf{b}^*$ can be calculated by the homogenization method, see, e.g. (3.4), (3.6). They are

$$a_{11}^* = 0.629416, \quad a_{12}^* = a_{21}^* = 0.258831, \quad a_{22}^* = 1.017663, \quad b_1^* = 1.147079, \quad b_2^* = 0.833333.$$

It is known that the first step of the upscaling method is to get the solution of the local problem. We remark here that the methods and error estimates we established in Section 2 and 3 are obtained under the assumption that the solutions of the local problems are analytically given. However, for numerical computations, these local problems have to be solved numerically. Therefore, it is important to analyze the error transmitted on the macroscale by discretizing the fine scale (see [1] for some detailed discussion on this topic). In our tests, the local problems (2.4) and (2.6) are solved on uniform triangle grids by using the Galerkin finite element method with linear base functions. Denote h_{cell} the size of triangle grids which we use to solve the local problems. The local problem discretizing error is fixed by keeping $\varepsilon/h_{\mathrm{cell}}$ to be constant. We denote h the considered grid block size in the following. Our numerical experiments are stated as the following four cases.

4.1. Case 1. $h = \varepsilon = 1, h_{\mathrm{cell}}$ reduces

The goal of the first series of numerical experiments is to check up the resonance error ε/h, which exists generally in the upscaling methods [35]. To do this, we set $h = \varepsilon = 1$ and reduce the h_{cell} to improve the

Table 1
Convergence of UM1: $\tilde{\mathbf{a}}$ to $\mathbf{a}^*$, $\tilde{\mathbf{b}}$ to $\mathbf{b}^*$; ($\varepsilon = h = 1$), h_{cell} reduces

h_{cell}	$\lvert\tilde{a}_{11} - a^*_{11}\rvert$	$\lvert\tilde{a}_{12} - a^*_{12}\rvert$	$\lvert\tilde{a}_{21} - a^*_{21}\rvert$	$\lvert\tilde{a}_{22} - a^*_{22}\rvert$	$\lvert\tilde{b}_1 - b^*_1\rvert$	$\lvert\tilde{b}_2 - b^*_2\rvert$
1/16	8.126e−02	2.576e−02	4.168e−02	1.397e−02	1.681e−03	3.771e−03
1/32	6.810e−02	1.725e−02	3.486e−02	1.023e−02	5.235e−03	3.175e−03
1/64	6.425e−02	1.505e−02	3.285e−02	9.289e−03	7.361e−03	3.150e−03
1/128	6.326e−02	1.449e−02	3.233e−02	9.048e−03	7.918e−03	3.167e−03
1/256	6.301e−02	1.435e−02	3.220e−02	8.988e−03	8.059e−03	3.173e−03
1/512	6.294e−02	1.432e−02	3.217e−02	8.973e−03	8.094e−03	3.175e−03

accuracy of the local problem resolving. The errors of $\tilde{\mathbf{a}}$ and $\tilde{\mathbf{b}}$ compared to $\mathbf{a}^*$ and $\mathbf{b}^*$ are presented in Table 1 for UM1 and Table 2 for UM2 corresponding. From the tables we see that the errors do not convergence to zero as grid refines. Evidently, the resonance error is dominating in this case (note that $\varepsilon/h = 1$). We also notice that UM1 loses the symmetry of $\tilde{a}$ while UM2 keeps well (note here $\varepsilon = 1$).

4.2. Case 2. $h = 1, \varepsilon$ reduces, $\varepsilon/h_{\text{cell}} = 16$

As shown by (3.8),(3.9), (3.10) and (3.11), one way of reducing the resonance error is to reduce the ratio ε/h. To show this, we set $h = 1$ and reduce ε from 1 to 1/32. Note that the discretization error of cell problems solving is fixed in the test because $\varepsilon/h_{\text{cell}} = 16$ is kept constant; hence, the error reduction is mainly due to the decrease of the resonance error. The errors of $\tilde{\mathbf{a}}$ and $\tilde{\mathbf{b}}$ compared to $\mathbf{a}^*$ and $\mathbf{b}^*$ are plotted in Fig. 1 for UM1, UM2 corresponding.

From the figure we see that the errors decrease as ε reduces. We also notice that for UM1, $\tilde{a}_{12} \neq \tilde{a}_{21}$, the symmetry does not hold. But, when ε reduces, the error between $\tilde{a}_{12}$ and $\tilde{a}_{21}$ decreases. This point can also be observed in the following tests where we keep $\varepsilon = 1/32$, hence $\tilde{a}_{12}$ looks very close to $\tilde{a}_{21}$.

Table 2
Convergence of UM2: $\tilde{\mathbf{a}}$ to $\mathbf{a}^*$, $\tilde{\mathbf{b}}$ to $\mathbf{b}^*$; ($\varepsilon = h = 1$), h_{cell} reduces

h_{cell}	$\lvert\tilde{a}_{11} - a^*_{11}\rvert$	$\lvert\tilde{a}_{12} - a^*_{12}\rvert$	$\lvert\tilde{a}_{21} - a^*_{21}\rvert$	$\lvert\tilde{a}_{22} - a^*_{22}\rvert$	$\lvert\tilde{b}_1 - b^*_1\rvert$	$\lvert\tilde{b}_2 - b^*_2\rvert$
1/16	7.532e−02	3.762e−02	3.762e−02	1.889e−02	1.162e−02	5.652e−03
1/32	6.206e−02	3.103e−02	3.103e−02	1.551e−02	9.627e−03	4.813e−03
1/64	5.822e−02	2.911e−02	2.911e−02	1.456e−02	9.299e−03	4.649e−03
1/128	5.723e−02	2.861e−02	2.861e−02	1.431e−02	9.237e−03	4.618e−03
1/256	5.698e−02	2.849e−02	2.849e−02	1.424e−02	9.223e−03	4.611e−03
1/512	5.692e−02	2.846e−02	2.846e−02	1.423e−02	9.219e−03	4.609e−03

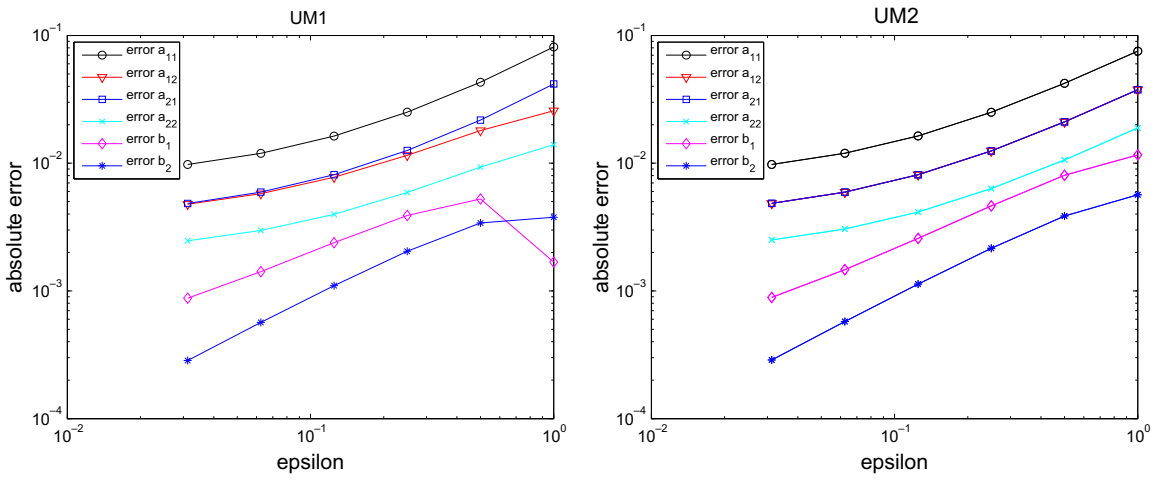

Fig. 1. Absolute error of UM1 (left) and UM2 (right).

4.3. Case 3. $\varepsilon = 1/32$, h reduces, $\varepsilon/h_{\text{cell}} = 12$

In this case, the numerical experiments are done by fixing $\varepsilon = 1/32$ and reducing h from 2 to 1/48. All considered domains are squares with the center point located at $(0.5, 0.5)$. The results are depicted in Fig. 2 for UM1, UM2 corresponding. Note that the discretization error of cell problems solving is still fixed in this case by keeping $\varepsilon/h_{\text{cell}}(= 12)$ constant.

It is obvious to see from the figure that the absolute errors of $\tilde{\mathbf{a}}$ and $\tilde{\mathbf{b}}$ compared to $\mathbf{a}^*$ and $\mathbf{b}^*$ increase when h decreases. As shown by (3.9), (3.10) and (3.11), the error between b_i^* and $\tilde{b}_i$ of UM1 and the errors of UM2 should increase as h reduces, while for the error between a_{ij}^* and $\tilde{a}_{ij}$ of UM1, in view of (3.8), there should have an equilibrium point of value h to make the error achieve the minimum. Unfortunately, we have not found the equilibrium point in our tests. This observation also shows that the resonance error is the leading error of UM1 and the error bound h term of UM1 almost does not take any affection. To show this more clearly, we design a series of experiments via reducing h and ε simultaneously and keeping $h = \varepsilon$ in the following case.

4.4. Case 4. $h(= \varepsilon)$ reduces, $\varepsilon/h_{\text{cell}} = 16$

In this case, we only carry out the experiments for UM1. The $h(= \varepsilon)$ reduces from 1 to 1/32 and when ε reduces we also change h_{cell} to keep $\varepsilon/h_{\text{cell}} = 16$. All considered domains are squares with center point located at $(0.5, 0.5)$. The results are listed in Table 3.

From the table we see that as $h(\varepsilon)$ reduces, the errors decrease slowly for $\tilde{a}_{11}$ and $\tilde{a}_{21}$, which is consistent with the previous theoretical result, e.g. (3.8). While, the errors increase slowly for other terms, instead of decrease as predicted by the error bound (3.8). However, when we move the considered squares to keep the left and bottom edges located on the y- and x-coordinates instead of keeping the center point of the squares

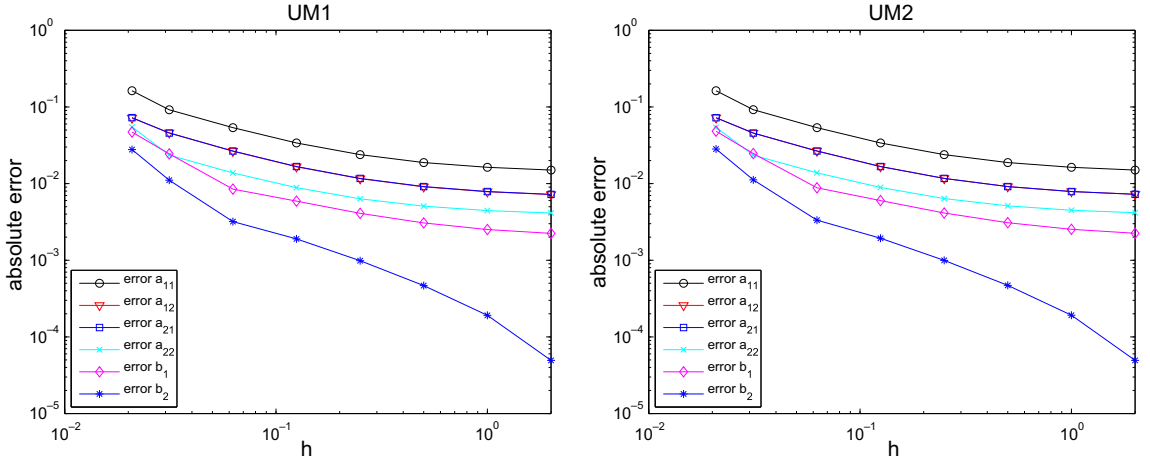

Fig. 2. Absolute error of UM1 (left) and UM2 (right).

Table 3
Convergence of UM1 of $\tilde{\mathbf{a}}$ to $\mathbf{a}^*$, $\tilde{\mathbf{b}}$ to $\mathbf{b}^*$ $(h = \varepsilon)$. $h(\varepsilon)$ reduces

$h(\varepsilon)$	$\lvert\tilde{a}_{11} - a_{11}^*\rvert$	$\lvert\tilde{a}_{12} - a_{12}^*\rvert$	$\lvert\tilde{a}_{21} - a_{21}^*\rvert$	$\lvert\tilde{a}_{22} - a_{22}^*\rvert$	$\lvert\tilde{b}_1 - b_1^*\rvert$	$\lvert\tilde{b}_2 - b_2^*\rvert$
1	9.727e−02	3.322e−02	4.847e−02	1.773e−02	2.782e−03	1.022e−03
1/2	9.409e−02	4.021e−02	4.692e−02	2.076e−02	3.744e−03	2.209e−03
1/4	9.290e−02	4.314e−02	4.627e−02	2.213e−02	6.605e−03	2.850e−03
1/8	9.240e−02	4.447e−02	4.598e−02	2.278e−02	7.929e−03	3.180e−03
1/16	9.218e−02	4.510e−02	4.584e−02	2.309e−02	8.563e−03	3.347e−03
1/32	9.211e−02	4.539e−02	4.576e−02	2.331e−02	8.856e−03	3.423e−03

located at (0.5,0.5), the opposite results happen. Indeed, we found the errors increase slowly for $\tilde{a}_{11}$ and $\tilde{a}_{21}$, while for others, the errors decrease slowly. The reason is not fully clear. Our tests show that these abnormal tiny errors may be caused by the round-off error.

4.5. Study on symmetry of $\tilde{\mathbf{a}}$ for random coefficients

As shown in Sections 4.1–4.3, UM2 gives a symmetric effective diffusive tensor $\tilde{\mathbf{a}}$, while UM1 does not. We also notice that when ε is small enough, the effective diffusive tensor generated by UM1 will be asymptotically symmetric (see Figs. 1 and 2). In this subsection, we do some tests to investigate the symmetry of $\tilde{\mathbf{a}}$ via UM1 for the model problem with random coefficients. To do this, we first generate two random log-normal functions $k_1(x)$ and $k_2(x)$ by using the moving ellipse average technique [12]. Then, we set

$$\mathbf{a}^{\varepsilon}(x) = k_1(x)\mathbf{E} \quad \text{and} \quad \mathbf{b}^{\varepsilon}(x) = \begin{pmatrix} k_2(x) \\ 0 \end{pmatrix},$$

where $\mathbf{E}$ represents the identity matrix in $\mathbb{R}^{2\times 2}$. A series of random functions $k_1(x)$ and $k_2(x)$ are generated by choosing different correlation lengths l_1, l_2 and variance of the logarithm of the functions σ^2 (see Table 4). With the same l_1, l_2 and σ^2, we generate $k_1(x)$ in the domain $(-0.25, 1.25) \times (-0.25, 1.25)$, and $k_2(x)$ in the domain $(0,1) \times (0,1)$. Therefore $k_1(x)$ and $k_2(x)$ are different in the considered domain $(0,1) \times (0,1)$. The random functions are defined in the 1024×1024 uniform mesh and the effective tensors are generated in the 64×64 uniform mesh. Since there are no exact homogenized coefficients to be compared in this case and the effective coefficients are different in each element of the mesh, we define the following relative error to indicate the extent of the asymmetry of $\tilde{\mathbf{a}}$:

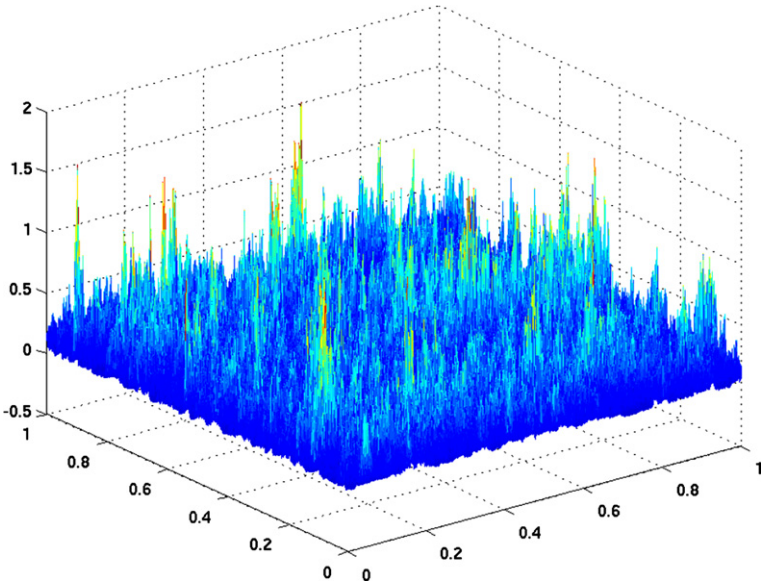

Fig. 3. The resolved velocity field $v_1^{\varepsilon}(x)$. The ratio of maximum to minimum is 4.265e+05. Case $l_1 = l_2 = 0.01$.

Table 4
Relative error between $\tilde{a}_{12}$ and $\tilde{a}_{21}$ for random coefficients

Relative Error	$\sigma^2 = 0.5$	$\sigma^2 = 1.0$	$\sigma^2 = 1.5$
$l_1 = 0.1, l_2 = 0.01$	0.71795	0.54662	0.50514
$l_1 = 0.01, l_2 = 0.001$	0.24894	0.17044	0.16941
$l_1 = 0.001, l_2 = 0.0001$	0.06148	0.04385	0.05073
$l_1 = 0.0001, l_2 = 0.00001$	0.01475	0.00797	0.00691

$$\text{Relative Error} = \frac{1}{M_i M_j} \sum_{i=1}^{M_i} \sum_{j=1}^{M_j} R_{ij}, \tag{4.3}$$

where R_{ij} is defined in element (i,j) with

$$R_{ij} = \frac{|\tilde{a}_{12} - \tilde{a}_{21}|}{(|\tilde{a}_{12}| + |\tilde{a}_{21}|)/2}, \tag{4.4}$$

and M_i and M_j represent the total numbers of elements in direction x_1 and x_2 respectively. Here $M_i = M_j = 64$. The results are shown in the following table.

From the table, we see that when the correlation lengths l_1, l_2 reduce, the error between $\tilde{a}_{12}$ and $\tilde{a}_{21}$ decreases. We also notice that when the variance increases, the error decreases for most of cases. It sounds that the higher oscillation of the coefficients, the better symmetry of the effective tensor, which is consistent with the previous observation for the periodic coefficients.

5. Application to the solute transport problem

In this section, we consider the application of the discussed upscaling methods (UMs) to the solute transport problem. For simplicity, the pore velocity $\mathbf{v}^\varepsilon(x)$ is determined by the following partial differential equation (the mass balance equation and Darcy's law, e.g. [5]):

$$\nabla \cdot \mathbf{v}^\varepsilon = q, \quad \mathbf{v}^\varepsilon = -\mathcal{K}(x)\nabla p \tag{5.1}$$

in the domain $\Omega = (0,1) \times (0,1)$ with the following boundary conditions:

$$p = 1 \quad \text{on } \Gamma_{\text{in}}, \quad p = 0 \quad \text{on } \Gamma_{\text{out}}, \; -\mathcal{K}(x)\nabla p \cdot \mathbf{n} = 0 \quad \text{on } \Gamma_N,$$

where $\Gamma_{\text{in}} = \{(x_1,x_2) : x_1 = 0, x_2 \in (0,1)\}$, $\Gamma_{\text{out}} = \{(x_1,x_2) : x_1 = 1, x_2 \in (0,1)\}$, and $\Gamma_N = \{(x_1,x_2) : x_1 \in (0,1), x_2 = 0 \text{ or} 1\}$. The boundary conditions for the pressure Eq. (5.1) represent a flow from Γ_{in} to Γ_{out} with noflow boundary conditions on Γ_N. The source q is generated by the same method as that for $\mathcal{K}(x)$ (see below), which is a random function. Thus, in the tests, the divergence of $\mathbf{b}^\varepsilon$ (here $\mathbf{v}^\varepsilon$) is not free. To solve the pressure Eq. (5.1), we utilize the linear Galerkin finite element method. We remark that to solve the pressure equation, it would be better to use the multiscale finite element method ([22]) or the mixed multiscale finite element method ([9]).

For the solute transport Eq. (1.2), we impose the following initial condition:

$$c(x,0) = 1 \text{ in } \Omega,$$

which means the simulation starts with a homogeneously polluted aquifer. The boundary condition on Γ_{in} and Γ_N is imposed with

$$(\mathbf{v}^\varepsilon c - \mathbf{D}^\varepsilon \nabla c) \cdot \mathbf{n} = 0 \quad \text{on } \Gamma_{\text{in}} \cup \Gamma_N,$$

which causes a flow of clean water through the inflow boundary. At the boundary Γ_{out}, we demand zero diffusive flux

$$-\mathbf{D}^\varepsilon \nabla c \cdot \mathbf{n} = 0 \quad \text{on } \Gamma_{\text{out}}.$$

In our test, we choose the dispersivities $\alpha_{\text{L}} = 0.1, \alpha_{\text{T}} = 0.01$. We emphasize the above values of the dispersivities represent the general case (see [16]). The dispersion tensor $\mathbf{D}^\varepsilon$ is computed via the formula (1.3).

Since there is no exact macro-scale solution for the random problem, we would compare the UM solutions to the oscillatory solution of the original equation. To do this, we solve (1.2) with corresponding initial-boundary conditions in a 1024×1024 mesh which we denote as DNS1024 in the following. The obtained solution c_h^ε is considered as the "exact" solution to compare with the UM solutions. The UM solutions, $\tilde{c}_h$, are solved in a coarse mesh (64×64) by UM1 and UM2 respectively. We also solve the Eq. (1.2) in a 64×64 mesh without doing upscaling procedure. That is to say, we do a direct numerical simulation in the coarse mesh, which neglects the fine scale oscillation in each grid. This method is denoted as DNS64.

As stated in Section 1, the oscillation of the velocity $\mathbf{v}^\varepsilon(x)$ hence diffusion coefficient $\mathbf{D}^\varepsilon(x)$ comes from the variability of the permeability $\mathcal{K}(x)$. Thus, it would be meaningful to consider different cases of $\mathcal{K}(x)$. Further, geostatistical models often suggest that the permeability field is generically a log-normal random field. To this end, we would like to consider the following two cases which represent isotropic and anisotropic heterogeneity respectively.

5.1. Case 1. Isotropic heterogeneity

We generate the random log-normal permeability field $k(x)$ by using the moving ellipse average technique [12] with the variance of the logarithm of the permeability $\sigma^2 = 1.5$, and the correlation lengths $l_1 = l_2 = 0.01$ (isotropic heterogeneity) in x_1 and x_2 directions, respectively. The ratio of maximum to minimum of one realization of the resulting permeability field in our numerical experiments is 2.198e + 09. Further, we choose the relative permeability tensor as $\mathcal{K}(x) = k(x)\mathbf{E}$. The resolved velocity $\mathbf{v}^\varepsilon$ is strongly varying; for example, see Fig. 3 below, where we depict the v_1^ε.

The concentration maps at times $t = 5$ and $t = 12$ are depicted in Figs. 4–7 for the methods DNS1024, UM1, UM2, DNS64 respectively. It can be seen that UM1 gives a better approximation to DNS1024 than

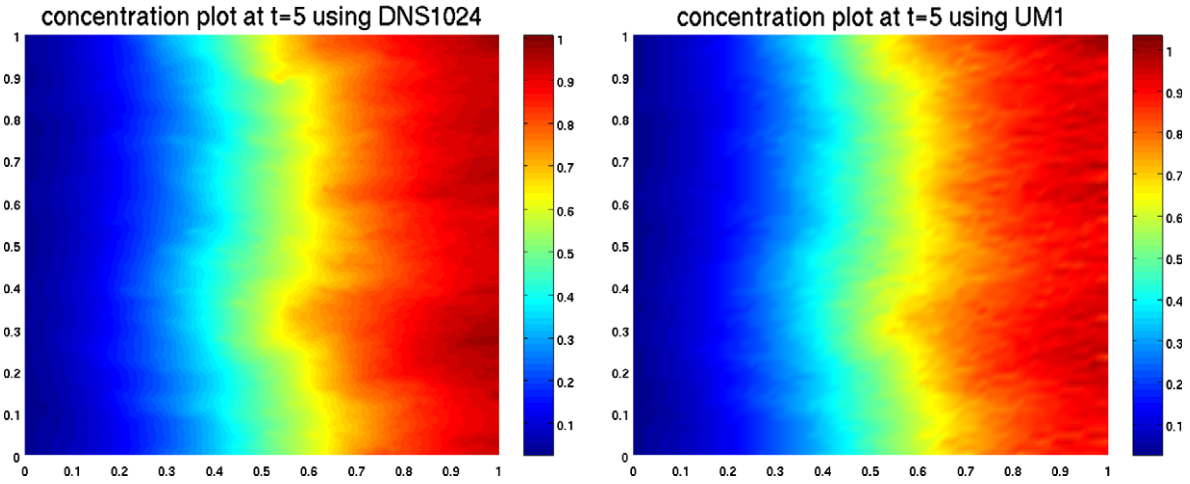

Fig. 4. Concentration maps at $t = 5$ for DNS1024 solution (left map), and UM1 solution (right map). Case $l_1 = l_2 = 0.01$.

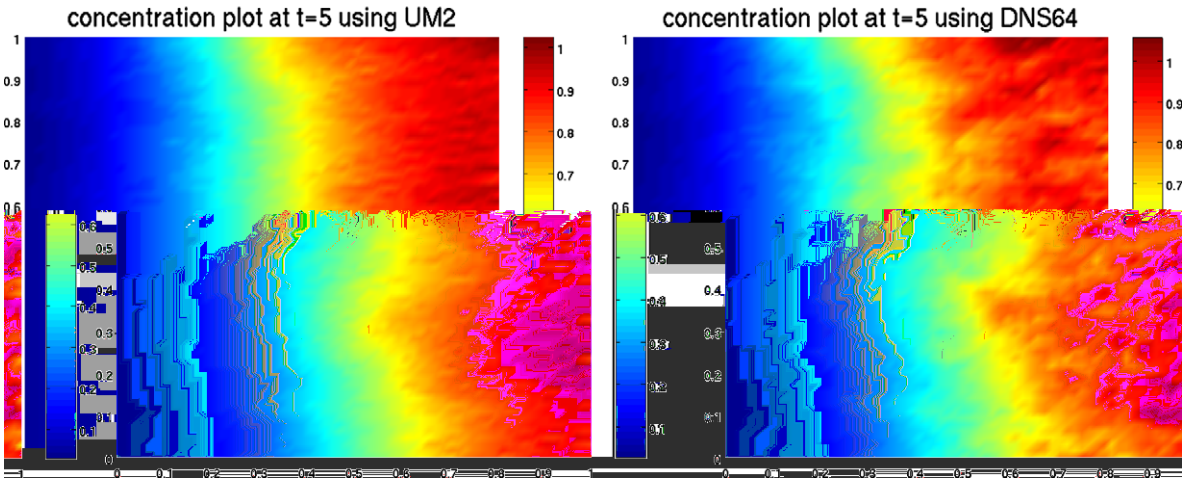

Fig. 5. Concentration maps at $t = 5$ for UM2 solution (left map), and DNS64 solution (right map). Case $l_1 = l_2 = 0.01$.

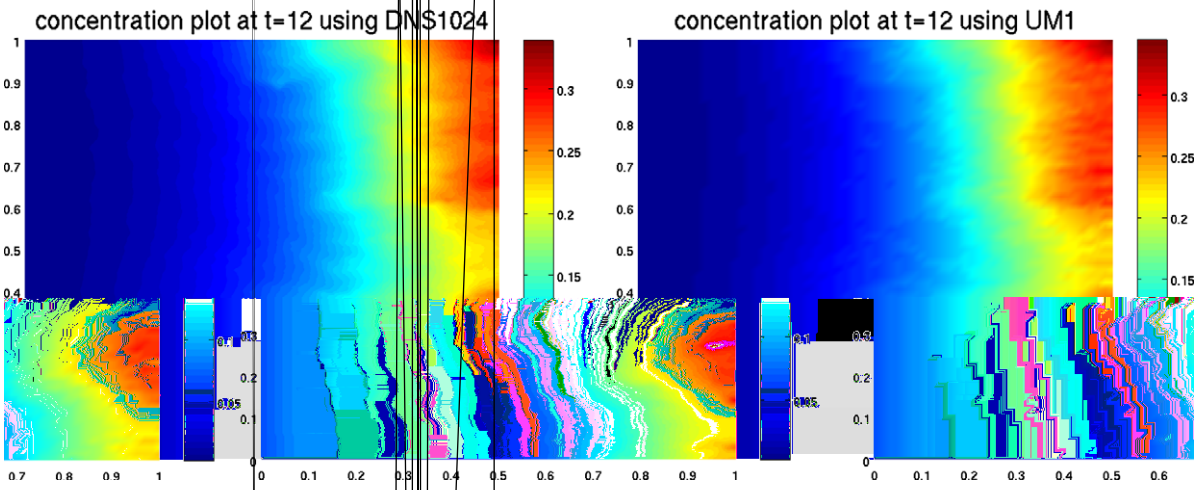

Fig. 6. Concentration maps at $t = 12$ for DNS1024 solution (left map), and UM1 solution (right map). Case $l_1 = l_2 = 0.01$.

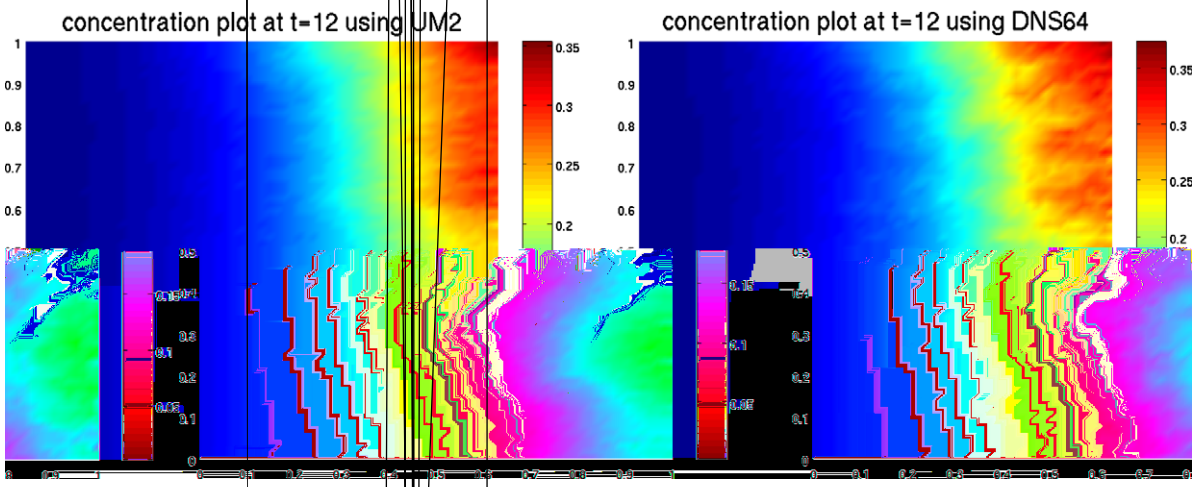

Fig. 7. Concentration maps at $t = 12$ for UM2 solution (left map), and DNS64 solution (right map). Case $l_1 = l_2 = 0.01$.

UM2, and UM2 gives a better approximation than DNS64 does. To see this more clearly, we plot the contour of the concentration c_h (corresponding c_h^ε) at times $t = 5$ and $t = 12$ in Fig. 8. We observe that both UM1 and UM2 solutions can capture the macro-behavior effectively while DNS64 gives an inaccurate approximation to the "exact" solution.

In practice, it is also important to predict the total pollutant mass in the whole domain. So, can the UMs capture the macro-quantity correctly? To answer this question, we compare the temporal decrease of the total pollutant mass $C^\varepsilon(t)$ for fine mesh and $\widetilde{C}(t)$ for coarse mesh respectively, where (see [33])

$$C^\varepsilon(t) = \int_\Omega c_h^\varepsilon(x)\mathrm{d}x, \quad \widetilde{C}(t) = \int_\Omega \tilde{c}_h(x)\mathrm{d}x.$$

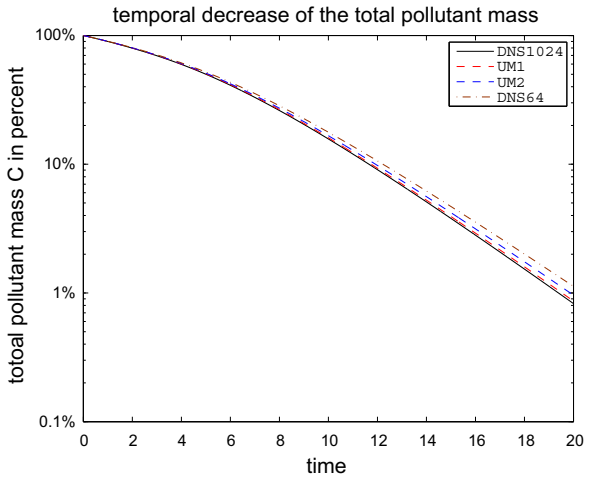

Fig. 9. The temporal decrease of the total mass $C^\varepsilon(t)$ and $\widetilde{C}(t)$ of UMs for isotropic heterogeneity. The black solid line stands for $C^\varepsilon(t)$, the red dash line stands for $\widetilde{C}(t)$ using UM1, the blue dash line stands for $\widetilde{C}(t)$ using UM2, and the maroon dash–dot line stands for $\widetilde{C}(t)$ using DNS64. Case $l_1 = l_2 = 0.01$. (For interpretation of the references to colour in this figure legend, the reader is referred to the web version of this article.)

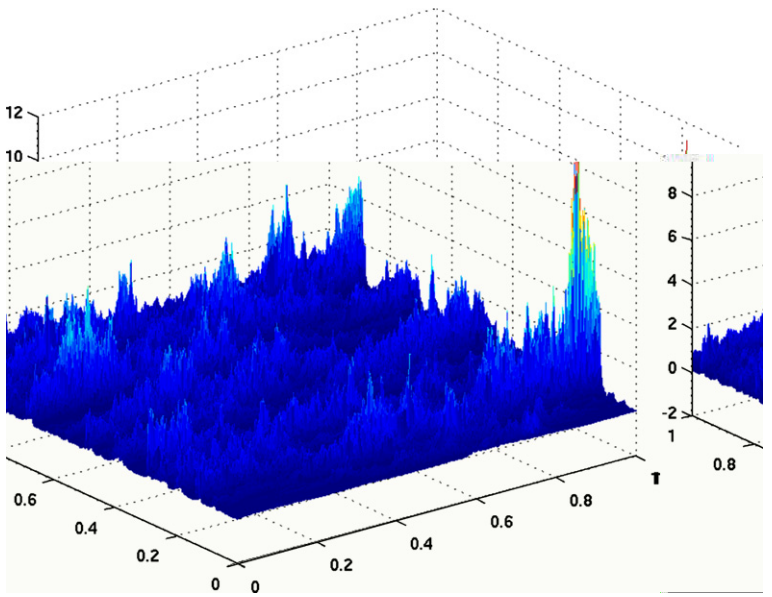

Fig. 10. The resolved velocity field $v_1^\varepsilon(x)$. The ratio of maximum to minimum is 1.532e+07. Case $l_1 = 0.1, l_2 = 0.01$.

We solve the problem to time $t = 20$. The decrease curves are depicted in Fig. 9 for the DNS1024, UM1, UM2, DNS64 respectively. We found that the $\widetilde{C}(t)$ by UM1 gives an excellent agreement to $C^{\varepsilon}(t)$, and UM2 gives an excellent agreement also but not as good as UM1. DNS64's also looks good but worse than UM1 and UM2 do.

5.2. Case 2. Anisotropic heterogeneity

In this case, we generate the random log-normal permeability field $k(x)$ with the correlation lengths $l_1 = 0.1$ and $l_2 = 0.01$ respectively, which represents the anisotropic heterogeneity. The ratio of maximum to minimum of one realization of the resulting permeability field in our numerical experiments is 1.334e + 09. Further, we choose the relative permeability tensor as $\mathcal{K}(x) = k(x)\mathbf{E}$. The resolved velocity $\mathbf{v}^{\varepsilon}$ is extremely varying; for example, see Fig. 10 below, where we depict the v_1^{ε}.

The concentration maps at times $t = 2$ and $t = 5$ are depicted in Figs. 11–14 for the methods DNS1024, UM1, UM2, DNS64 respectively. Again, we can see that UM1 gives an excellent approximation to the "exact" soltion, while DNS64 cannot move the solute concentration correctly. This observation can also be seen in Fig. 15 of the contour plots of the concentrations.

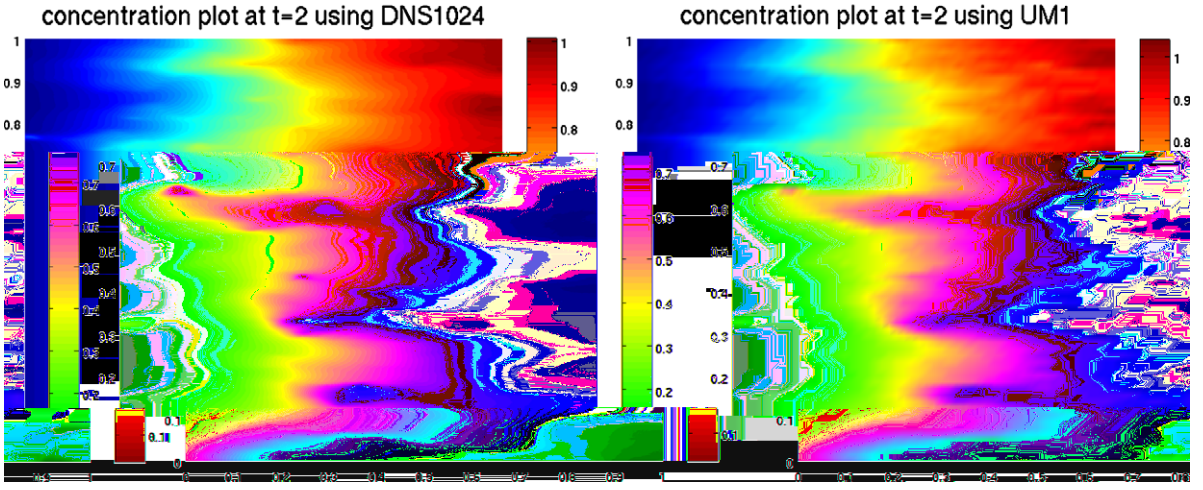

Fig. 11. Concentration maps at $t = 2$ for DNS1024 solution (left map), and UM1 solution (right map). Case $l_1 = 0.1, l_2 = 0.01$.

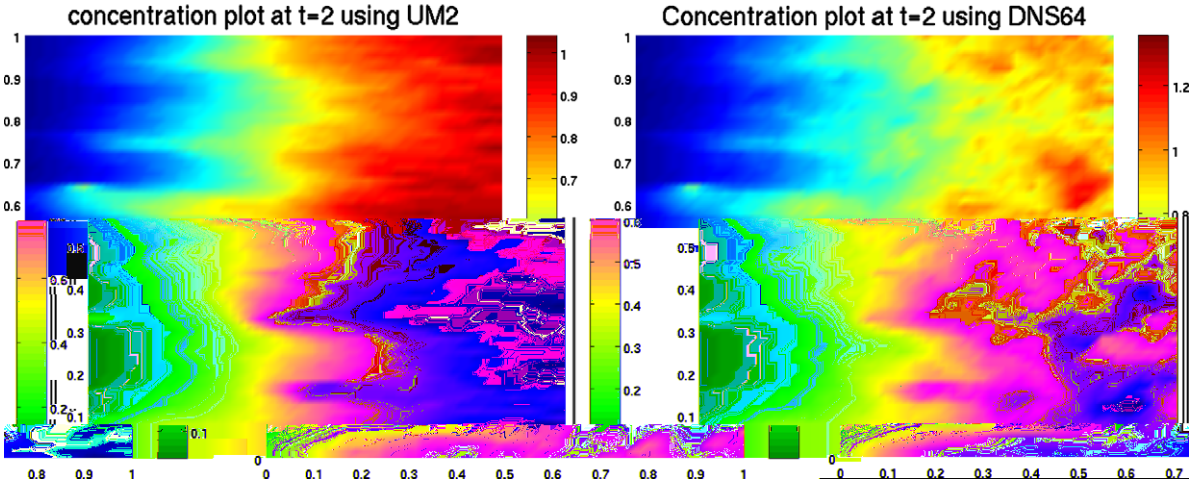

Fig. 12. Concentration maps at $t = 2$ for UM2 solution (left map), and DNS64 solution (right map). Case $l_1 = 0.1, l_2 = 0.01$.

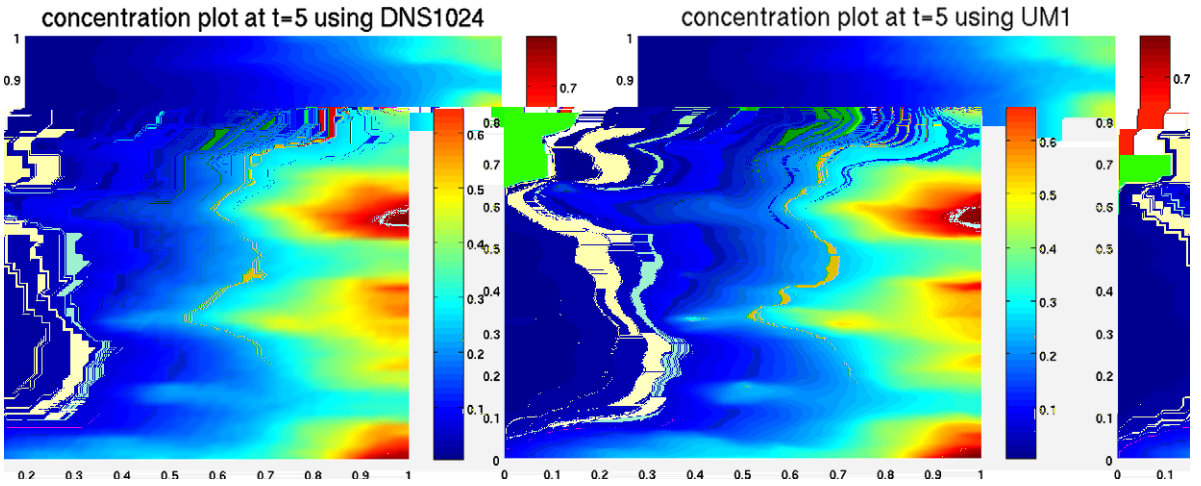

Fig. 13. Concentration maps at $t = 5$ for DNS1024 solution (left map), and UM1 solution (right map). Case $l_1 = 0.1, l_2 = 0.01$.

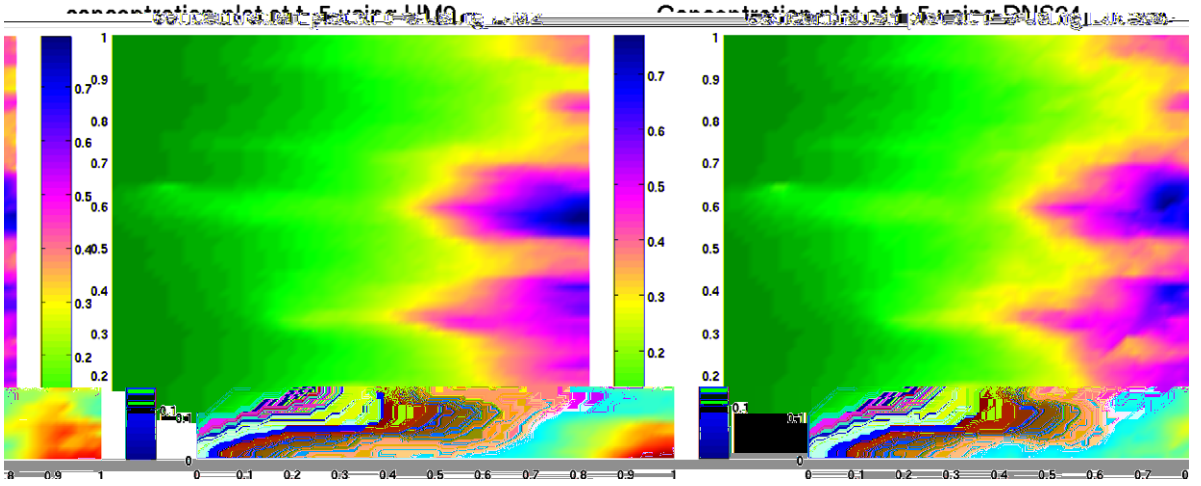

Fig. 14. Concentration maps at $t = 5$ for UM2 solution (left map), and DNS64 solution (right map). Case $l_1 = 0.1, l_2 = 0.01$.

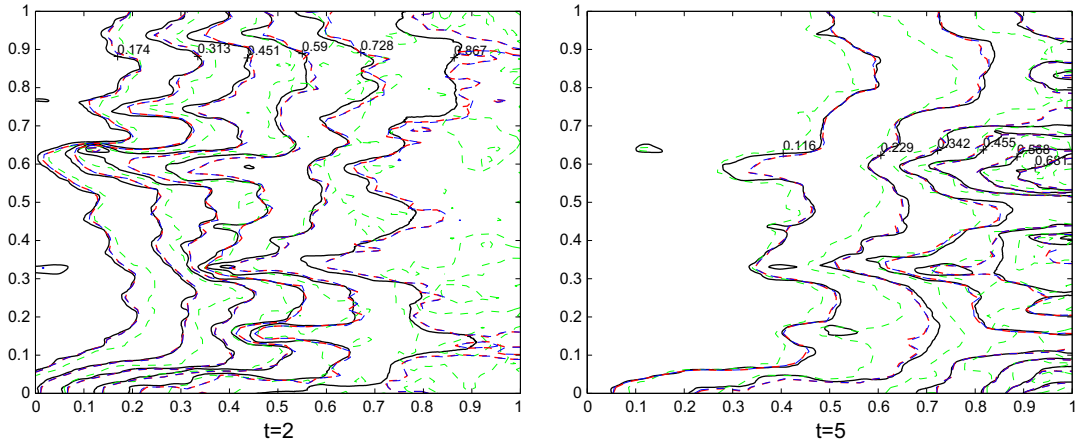

Fig. 15. The contour plots of c_h^ε and $\tilde{c}_h$ at $t = 2$ (left) and $t = 5$ (right). The black solid line stands for c_h^ε, the blue dash line stands for $\tilde{c}_h$ using UM1, the red dash line stands for $\tilde{c}_h$ using UM2, the green line stands for $\tilde{c}_h$ using DNS64. Case $l_1 = 0.1, l_2 = 0.01$. (For interpretation of the references to colour in this figure legend, the reader is referred to the web version of this article.)

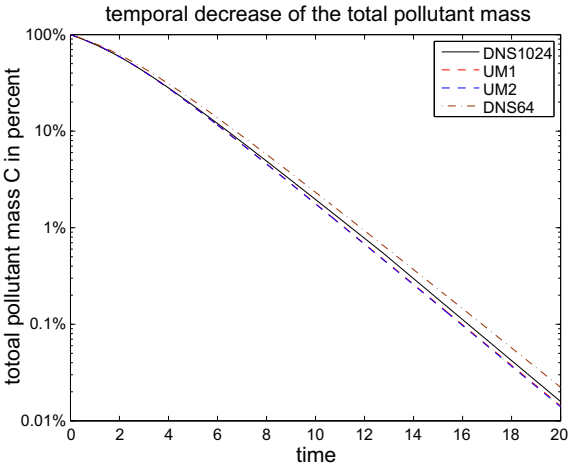

Fig. 16. The temporal decrease of the total mass $C^{\varepsilon}(t)$ and $\widetilde{C}(t)$ of UMs for anisotropic heterogeneity. The black solid line stands for $C^{\varepsilon}(t)$, the red dash line stands for $\widetilde{C}(t)$ using UM1, the blue dash line stands for $\widetilde{C}(t)$ using UM2, and the maroon dash-dot line stands for $\widetilde{C}(t)$ using DNS64. Case $l_1 = 0.1, l_2 = 0.01$. (For interpretation of the references to colour in this figure legend, the reader is referred to the web version of this article.)

We also compare the temporal decrease of the total pollutant mass $C^{\varepsilon}(t)$ for fine mesh and $\widetilde{C}(t)$ for coarse mesh respectively. The decrease curves are depicted in Fig. 16.

6. Conclusions

We have successfully developed a new upscaling method for solving the linear convection–diffusion type equations which arise in the studying of groundwater or solute transport in porous media. The main idea of the method is to define new effective coefficients based on the solutions of the local problems. Two different implementing methods are compared from error estimates to numerical experiments. The numerical tests of periodic cases demonstrate the obtained error estimates. Random cases show that the two methods are robust for more general cases. We emphasize that the numerical results show the upscaling method 1 (UM1) have a better performance in accuracy than the upscaling method 2 (UM2) does, while UM2 is more simple and easy to implement than the UM1.

Acknowledgments

The authors would like to thank the referees for their carefully reading and constructive comments that improved the paper.

Appendix A

Proof of Theorem 3.1. For simplicity, we only consider the two dimensional case where $d = 2$. We rewrite the formulae of a^*_{ij}, b^*_i as the following matrix (vector) form:

$$\mathbf{a}^* = \frac{1}{|Y|}\int_Y \mathbf{a}(y)(\mathbf{E} + \nabla_y \chi)\mathrm{d}y \tag{A.1}$$

and

$$\mathbf{b}^* = \frac{1}{|Y|}\int_Y \mathbf{a}(y)\nabla_y \eta \mathrm{d}y, \tag{A.2}$$

where $\mathbf{E}$ is the identity matrix and $\nabla_y\chi = (\nabla_y\chi^1, \nabla_y\chi^2)$. Note that the integration of a vector or a tensor means integrating each component separately. Furthermore, it follows from (3.5) that:

$$\nabla_y \cdot (\mathbf{a}(y)(\mathbf{E} + \nabla_y\chi)) = \mathbf{0}. \tag{A.3}$$

The following result (see [9, Lemma 4.9] or [15, Lemma 3.2]) will be used frequently in the next discussion. □

Lemma A.1. *Given domain K with $diam(K) = h$, let $\Phi(y) \in L^\infty(Y)$ defined in Y be a Y-periodic function in y, where Y is a unit cube. Then, we have*

$$\left| \frac{1}{|Y|} \int_Y \Phi(y)\mathrm{d}y - \langle \Phi(x/\varepsilon) \rangle_K \right| \leqslant C\varepsilon h^{-1},$$

where C is independent of ε and h.

To prove the estimate (3.9), we introduce the following auxiliary function:

$$\bar{p}_3^\varepsilon = 1 + \varepsilon\eta - \varepsilon\theta_3^\varepsilon,$$

where η is defined by (3.7) and θ_3^ε is the solution of

$$\begin{cases} -\nabla \cdot (\mathbf{a}(x/\varepsilon)\nabla\theta_3^\varepsilon) = 0 & \text{in } K, \\ \theta_3^\varepsilon = \eta(x/\varepsilon) & \text{on } \partial K. \end{cases} \tag{A.4}$$

It is easy to see that (cf. [23] or [9, Theorem 3.1])

$$\|\nabla\theta_3^\varepsilon\|_{0,K} \leqslant Ch^{1/2}\varepsilon^{-1/2}. \tag{A.5}$$

Moreover, we have

$$\|\theta_3^\varepsilon\|_{0,\infty,K} \leqslant C \tag{A.6}$$

by the Maximal Principle. The following lemma gives the H^1 and L^∞ errors between p_3^ε and $\bar{p}_3^\varepsilon$.

Lemma A.2. *There exists a constant C independent of ε, h such that*

$$\|\nabla(p_3^\varepsilon - \bar{p}_3^\varepsilon)\|_{0,K} \leqslant C\varepsilon \tag{A.7}$$

and

$$\|p_3^\varepsilon - \bar{p}_3^\varepsilon\|_{0,\infty,K} \leqslant C\varepsilon. \tag{A.8}$$

Proof of Lemma A.2. From the weak formulas of (2.4) and (A.4), for any $v \in H_0^1(K)$, we have

$$(\mathbf{a}(x/\varepsilon)\nabla p_3^\varepsilon + \mathbf{b}(x/\varepsilon)p_3^\varepsilon, \nabla v) = (\mathbf{b}^*, \nabla v),$$

and

$$(\mathbf{a}(x/\varepsilon)\nabla\theta_3^\varepsilon, \nabla v) = 0.$$

Denote $\varphi = p_3^\varepsilon - \bar{p}_3^\varepsilon$. Thus, we have

$$\begin{aligned} &(\mathbf{a}(x/\varepsilon)\nabla\varphi, \nabla v) + (\mathbf{b}(x/\varepsilon)\varphi, \nabla v) \\ &\qquad = -(\mathbf{a}(x/\varepsilon)\nabla(\varepsilon\eta) + \mathbf{b}(x/\varepsilon)\bar{p}_3^\varepsilon - \mathbf{b}^*, \nabla v) \\ &\qquad = -(\mathbf{H}(x/\varepsilon), \nabla v) - \varepsilon(\mathbf{b}(x/\varepsilon)(\eta - \theta_3^\varepsilon), \nabla v), \end{aligned} \tag{A.9}$$

where $\mathbf{H}(y) = (H_i(y))$ with

$$H_i(y) = a_{ij}(y)\frac{\partial\eta}{\partial y_j}(y) + b_i(y) - b_i^*.$$

From the definition of η, it follows that $\nabla \cdot \mathbf{H} = 0$, which yields:

$$(\mathbf{H}(x/\varepsilon), \nabla v) = 0.$$

Hence, we have

$$(\mathbf{a}(x/\varepsilon)\nabla\varphi, \nabla v) + (\mathbf{b}(x/\varepsilon)\varphi, \nabla v) = -\varepsilon(\mathbf{b}(x/\varepsilon)(\eta - \theta_3^\varepsilon), \nabla v). \tag{A.10}$$

Thus, in view of (A.6), we have (see [20, Corollary 8.7,Theorem 8.16])

$$\|\nabla\varphi\|_{0,K} \leqslant C\varepsilon \quad \text{and} \quad \|\varphi\|_{0,\infty,K} \leqslant C\varepsilon,$$

which ends the proof of Lemma A.2. □

In the next part, we prove the estimate (3.9). From the definitions of $\mathbf{b}^*$ and $\tilde{\mathbf{b}}$ (see (A.2) and (2.9)), we have

$$\mathbf{b}^* - \tilde{\mathbf{b}} = \frac{\langle \mathbf{a}^\varepsilon \nabla_y \eta + \mathbf{b}^\varepsilon \rangle_Y - \langle \mathbf{a}^\varepsilon \nabla \bar{p}_3^\varepsilon + \mathbf{b}^\varepsilon \bar{p}_3^\varepsilon \rangle_K}{\langle p_3^\varepsilon \rangle_K} + \frac{\mathbf{b}^*(\langle p_3^\varepsilon \rangle_K - 1) - \langle \mathbf{a}^\varepsilon \nabla (p_3^\varepsilon - \bar{p}_3^\varepsilon) + \mathbf{b}^\varepsilon (p_3^\varepsilon - \bar{p}_3^\varepsilon) \rangle_K}{\langle p_3^\varepsilon \rangle_K} =: \mathrm{I} + \mathrm{II}.$$

From (A.6) and (A.8), it follows that:

$$\langle p_3^\varepsilon \rangle_K = \langle \bar{p}_3^\varepsilon \rangle_K + \langle p_3^\varepsilon - \bar{p}_3^\varepsilon \rangle_K = 1 + \mathrm{O}(\varepsilon). \tag{A.11}$$

Hence, by use of Lemma A.2, it follows that:

$$|\mathrm{II}| \leqslant C_1\varepsilon + C_2\frac{\varepsilon}{h}.$$

Thus, in view of (A.11), it suffices to estimate $\langle \mathbf{a}^\varepsilon \nabla_y \eta + \mathbf{b}^\varepsilon \rangle_Y - \langle \mathbf{a}^\varepsilon \nabla \bar{p}_3^\varepsilon + \mathbf{b}^\varepsilon \bar{p}_3^\varepsilon \rangle_K$. A simple calculation shows

$$\begin{aligned}\langle \mathbf{a}^\varepsilon \nabla_y \eta + \mathbf{b}^\varepsilon \rangle_Y - \langle \mathbf{a}^\varepsilon \nabla \bar{p}_3^\varepsilon + \mathbf{b}^\varepsilon \bar{p}_3^\varepsilon \rangle_K &= (\langle \mathbf{a}^\varepsilon \nabla_y \eta \rangle_Y - \langle \mathbf{a}^\varepsilon \nabla_y \eta \rangle_K) + (\langle \mathbf{b}^\varepsilon \rangle_Y - \langle \mathbf{b}^\varepsilon \rangle_K) + \varepsilon \langle \mathbf{a}^\varepsilon \nabla \theta_3^\varepsilon \rangle_K - \varepsilon \langle \mathbf{b}^\varepsilon \eta \rangle_K \\ &\quad + \varepsilon \langle \mathbf{b}^\varepsilon \theta_3^\varepsilon \rangle_K =: I_1 + I_2 + I_3 + I_4 + I_5.\end{aligned}$$

From Lemma A.1, it follows that $|I_1| \leqslant C\varepsilon/h$ and $|I_2| \leqslant C\varepsilon/h$. Further, it is easy to see that $|I_4| \leqslant C\varepsilon$ and $|I_5| \leqslant C\varepsilon$.

The left task is to estimate $|I_3|$. Let $\phi_i^\varepsilon, i = 1, 2$ be the solution of the problem

$$\begin{cases} -\nabla \cdot (\mathbf{a}(x/\varepsilon)\nabla\phi_i^\varepsilon) = \nabla \cdot (\mathbf{a}(x/\varepsilon)\mathbf{e}_i) & \text{in } K, \\ \phi_i^\varepsilon = 0 & \text{on } \partial K. \end{cases} \tag{A.12}$$

It is easy to check that

$$\phi_i^\varepsilon = \varepsilon\chi^i(x/\varepsilon) - \varepsilon\theta_\chi^i, \ i = 1, 2, \tag{A.13}$$

where $\chi^i(y)$ is defined by (3.5) and θ_χ^i is the solution of

$$\begin{cases} -\nabla \cdot (\mathbf{a}(x/\varepsilon)\nabla\theta_\chi^i) = 0 & \text{in } K, \\ \theta_\chi^i = \chi^i(x/\varepsilon) & \text{on } \partial K \end{cases} \tag{A.14}$$

with (see [23] or [9, Theorem 3.1] also)

$$\|\nabla\theta_\chi^i\|_{0,K} \leqslant Ch^{1/2}\varepsilon^{-1/2}. \tag{A.15}$$

Since $\phi_i^\varepsilon \in H_0^1(K)$, we obtain from the variational formula of (A.4) that

$$\int_K \nabla\theta_3^\varepsilon \cdot (\mathbf{a}(x/\varepsilon)\nabla\phi_i^\varepsilon)\mathrm{d}x = 0, \quad i = 1, 2.$$

Note here we have used the symmetry of $\mathbf{a}(x/\varepsilon)$. Thus, by use of (A.13), it follows that:

$$\int_K \nabla\theta_3^\varepsilon \cdot (\mathbf{a}(x/\varepsilon)\nabla_y\chi^i)\mathrm{d}x = \varepsilon \int_K \nabla\theta_3^\varepsilon \cdot (\mathbf{a}(x/\varepsilon)\nabla\theta_\chi^i)\mathrm{d}x, \quad i = 1, 2. \tag{A.16}$$

Denote $\nabla\theta_\chi = (\nabla\theta_\chi^1, \nabla\theta_\chi^2)$. Then, from (A.16), we have

$$\int_K \mathbf{a}(x/\varepsilon)\nabla\theta_3^\varepsilon \mathrm{d}x = \int_K \nabla\theta_3^\varepsilon \cdot (\mathbf{a}(x/\varepsilon)(\mathbf{E} + \nabla_y\chi))\mathrm{d}x - \varepsilon \int_K \nabla\theta_3^\varepsilon \cdot (\mathbf{a}(x/\varepsilon)\nabla\boldsymbol{\theta}_\chi)\mathrm{d}x =: I_{31} + I_{32}. \tag{A.17}$$

From (A.5) and (A.15) and the Cauchy–Schwartz inequality, we have

$$|I_{32}| \leqslant C\varepsilon \|\nabla \theta_3^\varepsilon\|_{0,K} \|\nabla \boldsymbol{\theta}_\chi\|_{0,K} \leqslant Ch.$$

For the term I_{31}, in view of (A.3), integration by parts gives

$$|I_{31}| = \left| \int_{\partial K} \theta_3^\varepsilon \mathbf{n} \cdot (\mathbf{a}(x/\varepsilon)(\mathbf{E} + \nabla_y \chi)) \mathrm{d}\sigma \right| \leqslant Ch,$$

where $\mathbf{n}$ is the unit outward normal vector. Thus, we have

$$|I_3| \leqslant C\frac{\varepsilon}{h}.$$

The proof of the estimate (3.9) now is completed.

Next, we consider the errors between a_{i1}^* and $\tilde{a}_{i1}$, $i = 1, 2$. The others can be obtained by the same discussion. Denote $\bar{p}_1^\varepsilon = x_1 + \varepsilon\chi^1 + \varepsilon\eta x_1 - \varepsilon\theta_1^\varepsilon$, where χ^1, η are defined by (3.5) and (3.7), and θ_1^ε is the solution of

$$\begin{cases} -\nabla \cdot (\mathbf{a}(x/\varepsilon)\nabla\theta_1^\varepsilon) = 0 & \text{in } K, \\ \theta_1^\varepsilon = \chi^1 + \eta(x/\varepsilon)x_1 & \text{on } \partial K. \end{cases} \tag{A.18}$$

Similar to θ_3^ε, we have

$$\|\nabla\theta_1^\varepsilon\|_{0,K} \leqslant Ch^{1/2}\varepsilon^{-1/2}, \quad \|\theta_1^\varepsilon\|_{0,\infty,K} \leqslant C. \tag{A.19}$$

Moreover, we have the following Lemma which gives the H^1 and L^∞ errors between p_1^ε and $\bar{p}_1^\varepsilon$.

Lemma A.3. *There exist constants C_1, C_2 independent of ε, h such that*

$$\|\nabla(p_1^\varepsilon - \bar{p}_1^\varepsilon)\|_{0,K} \leqslant C_1\varepsilon + C_2h^2, \tag{A.20}$$

and

$$\|p_1^\varepsilon - \bar{p}_1^\varepsilon\|_{0,\infty,K} \leqslant C_1\varepsilon + C_2h. \tag{A.21}$$

Proof of Lemma A.3. It is obvious that $\nabla \cdot (\mathbf{a}^*\nabla x_1 + \mathbf{b}^*\langle x_1\rangle_K) = 0$. Thus, from the weak formulas of (2.4) and (A.18), for any $v \in H_0^1(K)$, we have

$$(\mathbf{a}(x/\varepsilon)\nabla p_1^\varepsilon + \mathbf{b}(x/\varepsilon)p_1^\varepsilon, \nabla v) = (\mathbf{a}^*\nabla x_1 + \mathbf{b}^*\langle x_1\rangle_K, \nabla v),$$

and

$$(\mathbf{a}(x/\varepsilon)\nabla\theta_1^\varepsilon, \nabla v) = 0.$$

Denote $\psi = p_1^\varepsilon - \bar{p}_1^\varepsilon$. Thus, we have

$$\begin{aligned} (\mathbf{a}(x/\varepsilon)\nabla\psi, \nabla v) + (\mathbf{b}(x/\varepsilon)\psi, \nabla v) &= -(\mathbf{a}(x/\varepsilon)\nabla(x_1 + \varepsilon\chi^1) - \mathbf{a}^*\mathbf{e}_1, \nabla v) - (\mathbf{a}(x/\varepsilon)\nabla(\varepsilon\eta x_1) \\ &\quad + \mathbf{b}(x/\varepsilon)\bar{p}_1^\varepsilon - \mathbf{b}^*x_1, \nabla v) - (\mathbf{b}^*(x_1 - \langle x_1\rangle_K), \nabla v) \\ &=: R_1 + R_2 + R_3. \end{aligned} \tag{A.22}$$

Denote $\mathbf{G} = (G_i)$ with

$$G_i(y) = a_{i1}(y) + a_{ik}\frac{\partial\chi^1}{\partial y_k}(y) - a_{i1}^*.$$

From the definition of χ^1, it follows that $\nabla \cdot \mathbf{G} = 0$ which yields $R_1 = 0$. The R_2 term can be estimated by the same way as that of Lemma A.2 (see the proof of Theorem 3.1 in [8] for details). For the term R_3, it is obvious that

$$\|x_1 - \langle x_1\rangle_K\|_{0,K} \leqslant Ch^2 \quad \text{and} \quad \|x_1 - \langle x_1\rangle_K\|_{0,\infty,K} \leqslant Ch.$$

Thus, in view of (A.19), we can show that (see [20, Corollary 8.7, Theorem 8.16])

$$\|\nabla\psi\|_{0,K} \leqslant C_1\varepsilon + C_2h^2 \quad \text{and} \quad \|\psi\|_{0,\infty,K} \leqslant C_1\varepsilon + C_2h,$$

which ends the proof of Lemma A.3. □

By use of Lemma A.3, it follows that:

$$\langle p_1^\varepsilon\rangle_K = \langle \bar{p}_1^\varepsilon\rangle_K + \langle p_1^\varepsilon - \bar{p}_1^\varepsilon\rangle_K = \langle x_1\rangle_K + \mathrm{O}(\varepsilon + h).$$

Thus, from Lemma A.1 and (3.9), we have

$$\tilde{\mathbf{b}}\langle p_1^\varepsilon\rangle_K = \langle \mathbf{a}^\varepsilon \nabla_y \eta + \mathbf{b}^\varepsilon\rangle_K \langle x_1\rangle_K + \mathrm{O}(\varepsilon + \frac{\varepsilon}{h}). \tag{A.23}$$

Finally, let's prove the errors between a_{i1}^* and $\tilde{a}_{i1}$, $i = 1, 2$. By use of (A.20), (A.21) and (A.23), a direct computation shows

$$\begin{aligned}\begin{pmatrix} a_{11}^* \\ a_{21}^* \end{pmatrix} - \begin{pmatrix} \tilde{a}_{11} \\ \tilde{a}_{21} \end{pmatrix} &= (\langle \mathbf{a}^\varepsilon(\mathbf{e}_1 + \nabla_y \chi^1)\rangle_Y - \langle \mathbf{a}^\varepsilon(\mathbf{e}_1 + \nabla_y \chi^1)\rangle_K) + (\langle \mathbf{a}^\varepsilon \nabla_y \eta + \mathbf{b}^\varepsilon\rangle_K \langle x_1\rangle_K - \langle (\mathbf{a}^\varepsilon \nabla_y \eta + \mathbf{b}^\varepsilon) x_1\rangle_K) \\ &\quad + \varepsilon \langle \mathbf{a}^\varepsilon \nabla \theta_1^\varepsilon\rangle_K + \mathrm{O}(h + \varepsilon + \tfrac{\varepsilon}{h}) =: \mathrm{Q}_1 + \mathrm{Q}_2 + \mathrm{Q}_3 + \mathrm{O}(h + \varepsilon + \tfrac{\varepsilon}{h})\end{aligned}$$

From Lemma A.1, it is clear that $|\mathrm{Q}_1| \leqslant C\varepsilon/h$. For Q_2, a simple calculation shows

$$|Q_2| = \frac{1}{|K|}\left|\int_K (\mathbf{a}^\varepsilon \nabla_y \eta + \mathbf{b}^\varepsilon)(\langle x_1\rangle_K - x_1)\mathrm{d}x\right| \leqslant Ch.$$

Further, a same discussion as that of I_3 yields that $|Q_3| \leqslant C\varepsilon/h$. Thus, we obtain the estimate (3.8). The proof of Theorem 3.1 now is completed. □

References

[1] A. Abdulle, On a priori error analysis of fully discrete heterogeneous multiscale FEM, Multiscale Model. Simul. 4 (2) (2005) 447–459.
[2] T. Arbogast, Implementation of a locally conservative numerical subgrid upscaling scheme for two-phase Darcy flow, Comput. Geosci. 6 (2002) 453–481.
[3] I. Babuska, G. Caloz, J. Osborn, Special finite element methods for a class of second order elliptic problems with rough coefficients, SIAM J. Numer. Anal. 31 (1994) 945–981.
[4] I. Babuska, J. Osborn, Generalized finite element methods: their performance and their relation to mixed methods, SIAM J. Numer. Anal. 20 (1983) 510–536.
[5] J. Bear, Dynamics of Fluids in Porous Media, American Elsevier, New York, 1972.
[6] A. Bensoussan, J.L. Lions, G. Papanicolaou, Asymptotic analysis for periodic structure volume 5 of Studies in Mathematics and Its Application, North-Holland Publ., New York, 1978.
[7] F. Brezzi, L.P. Franca, T.J.R. Hughes, A. Russo, $b = \int g$, Comput. Methods Appl. Mech. Eng. 145 (1997) 329–339.
[8] Z. Chen, W. Deng, H. Ye, A new upscaling method for the solute transport equations, Discrete Contin. Dyn. Syst. Ser. A 13 (4) (2005) 941–960.
[9] Z. Chen, T.Y. Hou, A mixed multisclae finite method for elliptic problemswith oscillating coefficients, Math. Comput. 72 (2002) 541–576.
[10] G. Dagan, Flow and Transport in Porous Formations, Springer-Verlag, Berlin Heidelberg, 1989.
[11] M. Dorobantu, B. Engquist, Wavelet-based numerical homogenization, SIAM J. Numer. Anal. 35 (1998) 540–559.
[12] L.J. Durlofsky, Numerical calculation of equivalent grid block permeability tensors for heterogeneous porous media, Water Resour. Res. 27 (1991) 699–708.
[13] W.E., B. Engquist, The heterogeneous multiscale methods, Commun. Math. Sci. 1 (2003) 87–132.
[14] W.E., P. Ming, P. Zhang, Analysis of the heterogeneous multiscale method for elliptic homogenization problems, J. Am. Math. Soc. 18 (2005) 121–156.
[15] Y. Efendiev, T.Y. Hou, X.H. Wu, Convergence of a nonconforming multiscale finite element method, SIAM J. Numer. Anal. 37 (2000) 888–910.
[16] E. Ewing, Aspects of upscaling in simulation of flow in porous media, Adv. Water Resour. 20 (1997) 349–358.
[17] C.L. Farmer, Upscaling: A review. In: Proceedings of the Institute of Computational Fluid Dynamics Conference on Numerical Methods for Fluid Dynamics, Oxford, UK, 2001.
[18] C. Farhat, I. Harari, L.P. Franca, The discontinuous enrichment method, Comput. Meth. Appl. Mech. Eng. 190 (2001) 6455–6479.
[19] J. Fish, Z. Yuan, Multiscale enrichment based on partition of unity, Inter. J. Numer. Meth. Eng. 62 (2005) 1341–1359.
[20] D. Gilbarg, N.S. Trudinger, Elliptic Partial Differential Equations of Second Order, Springer-Verlag, Berlin, 2001.
[21] U. Hornung (Ed.), Homogenization and Porous Media IAM, vol. 6, Springer-Verlag, Berlin, 1997.
[22] T.Y. Hou, X.H. Wu, A multiscale finite element method for elliptic problems in composite materials and porous media, J. Comput. Phys. 134 (1997) 169–189.
[23] T.Y. Hou, X.H. Wu, Z. Cai, Convergence of a multiscale finite element method for elliptic problems with rapidly oscillation coefficients, Math. Comput. 68 (1999) 913–943.

[24] T.J.R. Hughes, Multiscale phenomena: Green's functions, the Dirichlet to Neumann formulation, subgrid scale models bubbles and the origin of stabilized methods, Comput. Meth. Appl. Mech. Eng. 127 (1995) 387–401.
[25] V.V. Jikov, S.M. Kozlov, O.A. Oleinik, Homogenization of Differential Operators and Integral Functionals, Springer-Verlag, Berlin, 1994.
[26] P. Ming, X.Y. Yue, Numerical methods for multiscale elliptic problems, J. Comput. Phys. 214 (2006) 421–445.
[27] J.D. Moulton, J.E. Dendy, J.M. Hyman, The black box multigrid numerical homogenization algorithm, J. Comput. Phys. 141 (1998) 1–29.
[28] M. Panfilov, Macroscale Models of Flow through Highly Heterogeneous Porous Media, Kluwer, Dordrecht, 2000.
[29] Y. Rubin, J.J. Gomez-Hernandez, A stochastic approach to the problem of upscaling of conductivity in disordered media: Theory and unconditional numerical simulations, Water Resour. Res. 26 (1990) 691–701.
[30] Ph. Renard, G. de Marsily, Calculating effective permeability: a review, Adv. Water Resour. 20 (1997) 253–278.
[31] G. Sangalli, Capturing small scales in elliptic problems using a Residual-Free Bubbles finite element method, SIAM Multiscale Model. Simul. 1 (2003) 485–503.
[32] A.E. Scheidegger, General theory of dispersion in porous media, J. Geophys. Res. 66 (10) (1961) 3273–3278.
[33] C. Wagner, W. Kinzelbach, G. Wittum, A robust method for groundwater flow and transport problems, Numer. Math. 75 (1997) 523–545.
[34] X.H. Wen, J.J. Gomez-Hernandez, Upscaling hydraulic conductivities in heterogeneous media, J. Hydrol. 183 (1996) 9–32.
[35] X.H. Wu, Y. Efendiev, T.Y. Hou, Analysis of upscaling absolute permeability, Discrete Contin. Dyn. Syst. Ser. B 2 (2002) 185–204.